FBOTs and AT2018cow following electron-capture collapse of merged white dwarfs

Maxim Lyutikov

Department of Physics and Astronomy, Purdue University, 525 Northwestern Avenue, West Lafayette, IN 47907-2036 and

Silvia Toonen

Anton Pannekoek Institute for Astronomy, University of Amsterdam, P.O. Box 94249, 1090 GE, Amsterdam

ABSTRACT

We suggest that fast-rising blue optical transients (FBOTs) and the brightest event of the class AT2018cow result from an electron-capture collapse to a neutron star following a merger of a massive ONeMg white dwarf (WD) with another WD. Two distinct evolutionary channels lead to the disruption of the less massive WD during the merger and the formation of a shell burning non-degenerate star incorporating the ONeMg core. During the shell burning stage a large fraction of the envelope is lost to the wind, while mass and angular momentum are added to the core. As a result, the electron-capture collapse occurs with a small envelope mass, after $\sim 10^2 - 10^4$ years. During the formation of a neutron star as little as $\sim 10^{-2} M_{\odot}$ of the material is ejected at the bounce-off with mildly relativistic velocities and total energy \sim few 10⁵⁰ ergs. This ejecta becomes optically thin on a time scale of days - this is the FBOT. During the collapse, the neutron star is spun up and magnetic field is amplified. The ensuing fast magnetically-dominated relativistic wind from the newly formed neutron star shocks against the ejecta, and later against the wind. The radiation-dominated forward shock produces the long-lasting optical afterglow, while the termination shock of the relativistic wind produces the high energy emission in a manner similar to Pulsar Wind Nebulae. If the secondary WD was of the DA type, the wind will likely have $\sim 10^{-4} M_{\odot}$ of hydrogen; this explains the appearance of hydrogen late in the afterglow spectrum. The model explains many of the puzzling properties of FBOTs/AT2018cow: host galaxies, a fast and light anisotropic ejecta producing a bright optical peak, afterglow high energy emission of similar luminosity to the optical, and late infra-red features.

Subject headings: (stars:) white dwarfs; (stars:) supernovae: general; stars: neutron

1. Introduction

AT2018cow (Smartt et al. 2018; Prentice et al. 2018; Perley et al. 2018; Ho et al. 2019; Margutti et al. 2019) is a mysterious astrophysical event. It is likely to be the brightest member of the class of fast-rising blue optical transient (FBOT, Drout et al. 2014). AT2018cow seems to be at a cross-road of supernova explosions (and associated complicated nuclear reactions, neutrino transports physics), pulsars/magnetars, (early) pulsar wind nebulae (PWNe), possibly GRBs and, as we suggest in the present paper, the physics of white dwarf binaries.

AT2018cow had a few surprising features, the most important in our view being:

- the optical rise-time of ≤ 3 days; this is the order of magnitude shorter than the conventional Ni-powered supernovae
- the peak optical luminosity $\sim 4 \times 10^{44} \text{ erg s}^{-1}$; this exceeds the typical peak power of supernovae
- the X-ray emission of initial power $\sim 10^{43}~{\rm erg~s^{-1}}$ had an extra component at $t \le 15~{\rm days}$, peaking at $\sim 40~{\rm keV}$ (Fig. 6 in Margutti et al. 2019)

- the clear change of properties of the emission at ~ 20 days (Fig. 9 in Margutti et al. 2019)
- an indication of the rising IR component at $t \ge 30$ days (Fig. 5 in Perley et al. 2018)
- the bright radio emission $t \ge 80$ day peaking at $\sim 10^{10}$ Hz (Fig. 11 in Margutti et al. 2019)

These properties exclude normal Ni-powered supernovae and require a separate formation channel. We discuss one such possible channel in the present paper, trying to build a coherent model of AT2018cow.

2. The model: a specific channel of WD mergers

In this paper we discuss a scenario where fast-rising blue optical transients (FBOTs) are powered by the electron-capture collapse following a merger of a massive ONeMg white dwarf (WD) with another WD. Previously, the electron-capture collapse was mostly used in the accretion models (Canal & Schatzman 1976), hence the name Accretion Induced Collapse, AIC (see also Timmes & Woosley 1992; Miyaji et al. 1980; Nomoto & Kondo 1991; Kitaura et al. 2006; Jones et al. 2016). Some details of binary evolution and of the collapse in such systems were previously discussed by Lyutikov & Toonen (2017), see also Brooks et al. (2017); Ruiter et al. (2019); Yungelson & Kuranov (2017); Toonen et al. (2018); Schwab et al. (2016).

Let us outline the main stages (see Lyutikov & Toonen 2017, for a more detailed discussion); also Ruiter et al. (2019). An initial system with a primary mass $M_1 \sim 6-10\,M_\odot$ and a secondary mass $M_2 \sim 3-6\,M_\odot$ forms via two distinct evolutionary channels a double degenerate CO-ONeMg WD system. For a sufficiently large mass ratio $q \equiv M_2/M_1 > q_{crit} \sim 0.25$ (Marsh et al. 2004), the ensuing gravitational wave-driven mass transfer is unstable, whereby the less massive CO WD is disrupted on a few orbital time scales and forms a disk around the primary. (Possible detonation of the CO WD secondary would eject a small amount of mass, leaving the ONeMG core mostly intact Kashyap et al. 2018). Disk accretion at high rates creates a spreading layer - a belt-like structure on the surface of the primary (Inogamov & Sunyaev 1999; Balsara et al. 2009; Inogamov & Sunyaev 2010; Belyaev et al. 2013; Philippov et al. 2016). After the spreading is complete on viscose time scale of $\sim 10^4$ seconds (e.g., Shen et al. 2012), the resulting star of $\sim 2M_\odot$ consists of a slowly rotating degenerate ONeMg core, and a non-degenerate envelope rotating with a period of hundreds of seconds. The non-degenerate envelope expands to $R_* \sim$ few 10^9 cm. The star will emit near the Eddington limit and drive powerful winds. Angular momentum contained in the shell will be both lost to the wind and transported to the core through the (turbulent) boundary layer.

The merger product ignites shell CO burning, adding mass to the degenerate core; at the same time, mass and angular momentum are lost due to powerful winds. For an ONeMg WD sufficiently close to the Chandrasekhar mass, an electron-capture/accretion induced collapse follows after $\sim 10^2 - 10^4$ years. During the collapse, the magnetic field is amplified (Mösta et al. 2015), and the neutron star is spun to millisecond periods.

To estimates the resulting magnetic field and the spin frequency, we note that during collapse of a core rotating initially with a spin frequency Ω and collapsing by a factor $\eta_c \sim 100$ (from a few thousand kilometers to a few tens), the final neutron star will rotate with $\omega_c \sim \eta_c^2 \Omega$. The ratio $\omega/\Omega = \eta_c^2 \sim 10^4$ also estimates by how much magnetic field is twisted during the collapse.

Thus, the final toroidal magnetic field can be $\sim 10^4$ times higher than the poloidal one. In addition, the poloidal magnetic field will be amplified by flux conservation. For example, if we start with $B_{WD} \sim 10^6$ G, flux conservation will give a factor $\eta_c^2 \approx 10^4$, while differential rotation will further boost that by $\sim 10^4$, reaching magnetar-like values of $B \geq B_Q$, $B_Q = m_e^2 c^3/(e\hbar)$.

As a result, the newly born spinning neutron star will produce a long lasting relativistic wind, that first shocks against the ejecta material and later on against the wind material lost during the shell-burning stage. The highly magnetized relativistic wind produced by a central neutron star will interact with the fairly dense newly ejected material and dense pre-AIC wind, producing an X-ray afterglow at the highly magnetized reverse shock, in a way similar to the case of afterglows from long GRBs, as suggested by Lyutikov & Camilo Jaramillo (2017).

In Fig. 1 we picture the immediate surrounding of an FBOT at times \sim days-weeks after the collapse. This picture is our working model.

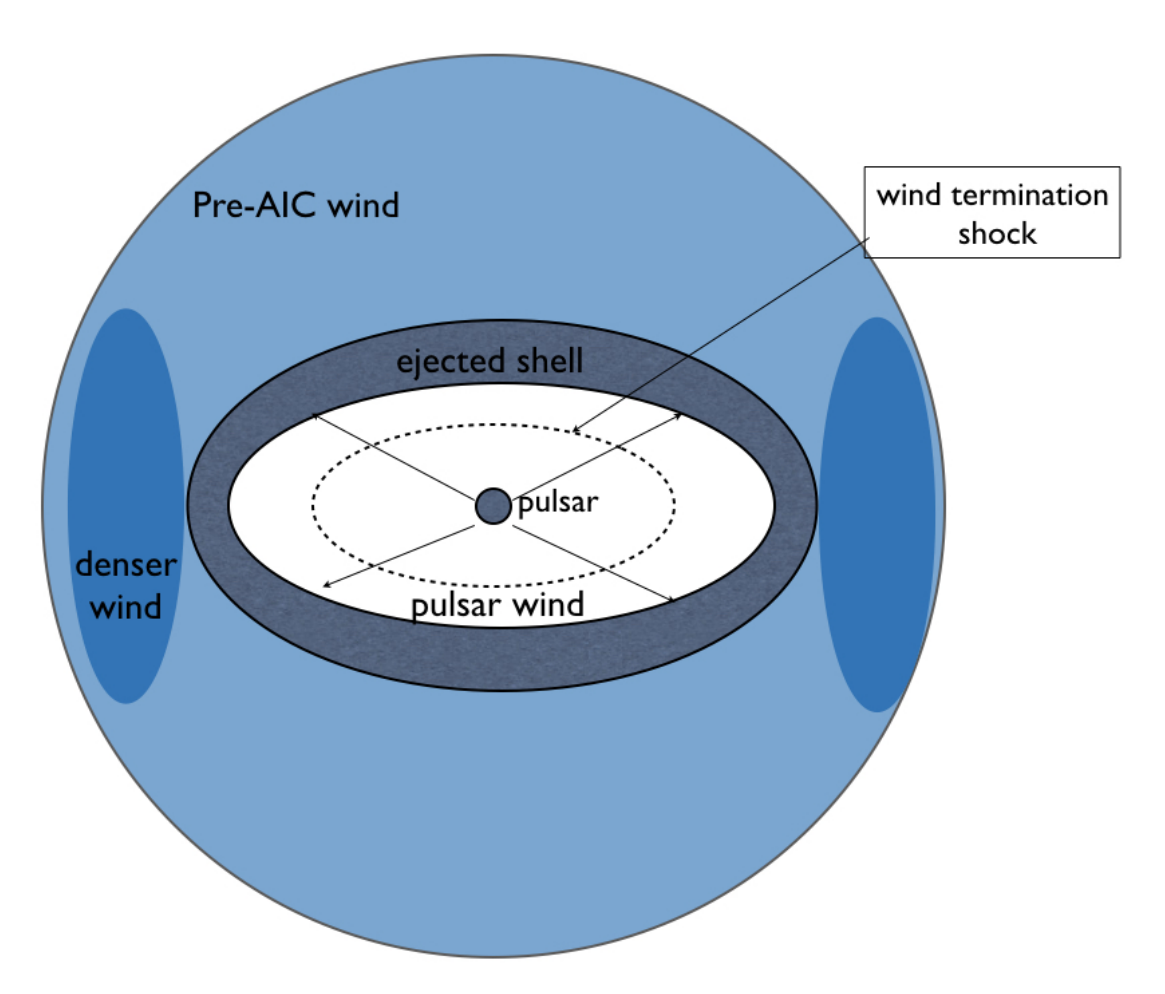


Fig. 1.— Immediate surrounding of a FBOTs: the remaining NS generates anisotropic pulsar-like wind (highly relativistic, highly magnetized with power $\sim \sin^2 \theta$), that interacts with the bounced-ejected shell, and the preceding wind from the shell burning stage. The pulsar winds, the ejected shell and the pre-explosion wind are all expected to be equatorially collimated.

The key point of the model is that a merger of a heavy ONeMg WD with another WD, and ensuring mass loss during the shell burning stage, results in a collapse of the core surrounded by a fairly light envelope, tens of percent of

 M_{\odot} at most. Depending on the particular collapse time one expects few cases when the AIC happens right before the shell burning is about to end. This would produce fast ejecta with small mass and leads to AT2018cow-like events. In other cases, envelopes of few tenths of solar masses are ejected, producing longer and less bright transients, which are still fast and luminous if compared with conventional supernovae.

In addition to spinning up the core, a large amount of angular momentum of the shell (disrupted secondary WD) is lost to the wind. As a result the AIC can be direct, without formation of the accretion disk. In this case the newly born neutron star looses most if its rotational energy to the fast, relativistic wind. For shorter shell-burning stage, there is too much angular momentum in the shell, that leads to the formation of the accretion disk, that spins down the central neutron star in a propeller stage. As a result, a large fraction of the energy is deposited into relatively slow, matter-dominated wind with low radiation efficiency.

3. The pre-collapse wind and the ejecta

3.1. Pre-collapse wind

Let's assume that the post-merger/shell-burning star launches a wind with velocity V_w . After time t_w the edge of wind reaches radius $r_{max} = R_* + V_w t_w$. For a total mass in the wind M_{env} we find

$$\rho_w = \frac{\dot{M}}{4\pi r^2 V_w}$$

$$M_{env} = \int_{R_*}^{R_* + V_w t_w} \rho_w 4\pi r^2 dr = \dot{M} t_w$$

$$t_w = \frac{M_{env}}{\dot{M}}$$
(1)

For mass loss rate of $\dot{M}=10^{-3}M_{\odot}~\rm{yr^{-1}}$ and total mass in the envelope of $\sim 0.5M_{\odot}$ this stage lasts $t_w\sim 5\times 10^2~\rm{yrs}$; we adopt notation $x_n=X/10^n$.

Optical depth to Thomson scattering trough the wind is ~ 1 at

$$r_w = \frac{\sigma_R \dot{M}}{4\pi m_p V_w} = 2 \times 10^{13} \dot{m}_{-3} V_{w,8}^{-1} \text{cm}$$
 (2)

In fact, the wind is composed of the WD material rich in heavy elements. Thus, it's opacity is similar to the case of type Ia supernova - it is dominated by line transitions, in expanding wind and can be an order of magnitude higher than free-free scattering (Karp et al. 1977; Pinto & Eastman 2000; Höflich et al. 1998).

3.2. Ejecta

As the shell is accreted onto the proto-neutron star, a narrow outer layer will be ejected. Studies of the AIC ejected mass predict $\sim 10^{-3} - 10^{-1} M_{\odot}$ ejected (Woosley & Baron 1992; Fryer et al. 1999; Abdikamalov et al. 2010; Sharon & Kushnir 2019).

These studies were mostly concerned with single degenerate scenario of AIC, basically with no envelope. It is not clear how a presence of a tenuous envelope, of few $0.1M_{\odot}$, would affect the ejecta mass. Let us assume, for a particular

case of AT2018cow, a bounced ejected mass of M_{ej} , with maximal velocity $V_{ej,0}$. For homologous expansion with $v \propto r$, the energy in the ejected part is

$$E_{ej} = \frac{3}{10} M_{ej} V_{ej,0}^2 \tag{3}$$

Before the ejecta slows down due to the interaction with the pre-existing wind, its density evolves according to

$$\rho_{ej} = \frac{3}{4\pi} \frac{M_{ej}}{(V_{ej,0} t_{ej})^3} \tag{4}$$

where $V_{ej,0}$ is the maximum velocity of the ejecta.

For numerical estimates we chose $M_{ej} \approx 10^{-2} m_{ej,-2} M_{\odot}$. (Many of the final relations depend weakly on ejecta mass, $\propto M_{ej}^{1/4}$, e.g., Eq. (21) and 23)). The velocity of the ejecta will be related to the escape velocity from the proto-neutron star,

$$V_{ej,0} \approx \sqrt{\frac{GM_{NS}}{R_{proto-NS}}} = 7 \times 10^9 \text{cms}^{-1} = 0.26c$$
 (5)

for a proto-neutron star radius of $R_{proto-NS}=30$ km. The ejecta energy is then $E_{ej}\approx 4\times 10^{50}m_{ej,-2}$ erg. Thus, our model naturally produces fast and light ejecta.

3.3. Ejecta-wind interaction

The ejecta will launch a forward shock into the pre-explosion wind. As the shock propagates through the wind the accumulated mass is then

$$M_{acc} \approx \dot{M}t \frac{V_{ej,0}}{V_{vv}} \tag{6}$$

It becomes equal the ejecta mass at

$$t_{slow} = \frac{M_{ej}}{\dot{M}} \frac{V_w}{V_{ej,0}} \to 4 \times 10^6 m_{ej,-2} V_{w,8} \dot{m}_{-3}^{-1} sec$$
 (7)

Thus, the external wind has little effect on the ejecta until approximately a month after the explosion. Before that the ejecta is in free expansion stage.

This will be approximately the time that the NS-driven shock exits the ejecta and enters the wind. We associate this with the transition of the afterglow properties at ~ 20 days (Margutti et al. 2019).

4. Optical transient

4.1. Optical emission-I: expansion of the ejecta

As discussed by Drout et al. (2014), fast optical transients can be powered either by the thermal energy of a low mass ejected envelope or by the central engine. In the first case The Thomson optical depth through ejecta is

$$\tau_{ej} = \frac{\rho_{ej}}{m_p} \sigma_T V_{ej,0} t = \frac{3}{4\pi} \frac{M_{ej} \sigma_T}{m_p (V_{ej,0} t)^2} = 3m_{ej,-2} t_d^{-2}$$
(8)

where t_d is time in days since the explosion. The surface $\tau = 1$ evolves with time according to

$$r_{ej,\tau=1} = V_0 t \left(1 - \frac{2\pi}{5} \frac{m_p V_0^4}{E_{ej} \sigma_T} \right) \tag{9}$$

It reaches maximum at

$$t_{ej,max} = \sqrt{\frac{5}{6\pi}} \sqrt{E_{ej}\sigma_T m_p V_0^4} \approx 1 m_{ej,-2}^{1/2} \text{day}$$

$$r_{ej,max} = \sqrt{\frac{10}{27\pi}} \sqrt{E_{ej}\sigma_T m_p V_0^2} \approx 5 \times 10^{14} m_{ej,-2}^{1/2} \text{cm}$$
(10)

This explains the short rise time of the transient. Also note that radius (10) is larger than the radius (2) when the wind becomes optically thin. Thus, the maximum of the ejecta emission is not affected by scattering in the pre-explosion wind.

In fact, for the expanding optically thick plasma the peak in luminosity will appears before the shell becomes optically thin due to the fact that photons diffuse out somewhat faster (Arnett 1982). The peak time is

$$t_{pk} \approx \sqrt{\frac{M_{ej}\kappa}{4\pi V_{ej,0}c}} \approx 0.4 m_{ej,-2} \text{days}$$
 (11)

where $\kappa \approx 0.1 \text{ cm}^2 \text{ g}^{-1}$ is an estimate of the effective opacity due to electron scattering. Estimates (8) and (11) explain the short rise time of the optical light curve.

The free-free emission of the optically thin part of the ejecta is fairly small,

$$L_{ej,ff} \approx j_{ff} n_{ej}^2 (V_{ej,0} t)^3 = 4 \times 10^{39} \text{erg s}^{-1} m_{ej,-2}^2 T_4^{1/2} t_d^{-3}$$
$$j_{ff} = 2.4 \times 10^{-27} \sqrt{T} n^2$$
(12)

where j_{ff} is free-free emissivity (Lang 1999). Thus, we associated the early fast optical transient with the emission of the ejected shell.

4.2. Optical emission-II: forward shock from the NS-driven wind

The NS wind is shocked at the termination shock and will also produce a forward shock. Similar amount of energy will be dissipated in both shocks. Particles accelerated at the termination shock produces the non-thermal X-ray emission, while the forward shock will produce the long lasting optical emission (in addition to the emission produced by the ejecta).

Let us first consider the forward shock emission. The forward shock initially propagates through the ejecta, and later-on through the pre-explosion wind. The shock driven by the NS wind will be modified by radiation pressure, (Weaver 1976; Budnik et al. 2010; Ofek et al. 2010; Lyutikov 2018). The observed properties of mildly relativistic shocks are fairly complicated and often have steep dependence on the underlying parameters due to steep dependence of photon production rates, phone escape and pair production on the plasma properties. Qualitatively, radiation-dominated shocks can temporarily reach temperature exceeding the shock jump conditions (even taking into account radiation pressure). For fast photon production this may results in isothermal jumps (Landau & Lifshitz 1959; Lyutikov 2018), in which case the peak temperature exceeds the final temperature by a factor of a few. For slow photon production the temperature peak may exceed the final temperature by a large amount (Ito et al. 2018; Ioka et al. 2018).

Let us give here an order-of-magnitude estimate of the *final* post-shock temperature in strongly radiationally-dominated shock. The post shock pressure is

$$p_{FS} \sim \frac{L_w}{4\pi R_{PWN}^2 c} = \frac{\sqrt{3}}{16\pi} \frac{\sqrt{L_{w,0} M_{ej}}}{\sqrt{c V_{ej}^{3/2} t^{5/2}}}$$
 (13)

The post-shock pressure is contributed both by matter pressure, $\sim nT$ and radiation pressure $\sim 4\sigma_{SB}T^4/c$. Radiation pressure dominates for (Weaver 1976; Budnik et al. 2010; Ofek et al. 2010; Lyutikov 2018)

$$V_s \gg \frac{(\rho \lambda_C^3)^{1/6} c}{m_e \mu^{2/3}} \approx 10^5 m_{ej,-2}^{1/6} t_d^{-1/2} \text{cm s}^{-1}$$
 (14)

where $\lambda_C = \hbar/(m_e c)$ and $\mu = m_p/m_e$. Comparing with (22) we conclude that the forward shock is radiation-dominated with post-shock temperature (far downstream!)

$$T_{FS} \approx \left(\frac{cL_{w,0}M_{ej}}{\sigma_{SB}^2 V_{ej,0}^3 t^5}\right)^{1/8} = 4 \times 10^4 \, m_{ej,-2} t_d^{-5/8} \text{K}$$
 (15)

This matches the observed temperatures at early times, both in value and (presumably) the temporal decrease (Margutti et al. 2019).

On the other hand, radiation-dominated shocks require sufficiently high optical depth, at least of the order of $\tau \sim c/V_s$, while final stationary configurations may be reached at optical depths of thousands (Ioka et al. 2018). This is not really satisfied in the particular case: from $r\sigma_T n \sim c/V_s$, with V_s given by (22) and density by (4), the condition $\tau \sim c/V_s$ is satisfied for

$$t \le \frac{L_{w,0}^{1/3} M_{ej}^{1/3} \sigma_T^{2/3}}{m_p^{2/3} cV_0} = 0.1 m_{ej,-2}^{1/3} \,\text{days}$$
(16)

Thus, only at very early times the shock is highly radiation-dominated.

At the moment of shock breakout, at $t \le 1$ day, we expect an X-ray flash with duration $\sim 10^4$ seconds, Eq. (16) and luminosities $\sim 10^{42} - 10^{43}$ erg s⁻¹ (e.g., Svirski & Nakar 2014). Later on, after the shock is no longer radiation dominated, the post-shock temperature evaluates to

$$T_s = \frac{3}{16} m_p V_s^2 \approx \frac{m_p L_{w,0}^{1/2} V_0^{3/2} \sqrt{t}}{\sqrt{c M_{ej}}} = 5 \times 10^5 t_d^{1/2} m_{ej,-2}^{-1/2} \text{eV}.$$
 (17)

The corresponding free-free luminosity is far too small $\sim 10^{35} m_{ej,-2}^{7/4} t_d^{-11/4} {\rm \ erg \ s^{-1}}$.

4.3. Anisotropy

Thus, optical emission is puzzling - it is hard to see how requirement of radiation-modified shocks (and hence large optical depth) can be reconciled with short transient time scales (and hence small optical depth). A possible answer is anisotropy. All the ingredients - pre-collapse wind, ejecta and the NS wind are expected to be anisotropic, see Fig. 1. First, the wind is launched by star that rotates with nearly critical velocity. Even Solar wind is highly anisotropic: slow and dense in the equatorial sector and fast in the polar regions (with approximately constant $d\dot{M}/d\Omega$). Second, the newly formed NS can, under certain parameters, be nearly critically spinning, so that the ejecta is anisotropic as well (see Lyutikov & Toonen 2017). Third, the remaining NS's wind is equatorially collimated, with power $\propto \sin^2 \theta$ (Michel 1973).

There are strong observational arguments in favor of anisotropy. First, hydrogen and helium lines show spectral asymmetry, with a tail towards longer wavelengths (Margutti et al. 2019). This can be explained if the line of sight samples unevenly the ejecta.

Anisotropic ejecta can also reconcile the requirements of low ejecta mass, $\sim 10^{-2} M_{\odot}$ (and hence early transparency) and the requirement of larger ejecta mass, to keep the NS wind-generated forward shock to be radiatively dominated, which would nicely explain the optical temperature, Eq. (15).

An alternative possibility is that the later optical emission originates as a synchrotron emission from particles accelerated at the forward shock. One can construct a model of particle acceleration at the forward shock following the standard GRB parametrization (e.g., Piran 2004), with $\epsilon_B \sim 10^{-4}$, $\gamma \sim 10^3$, in the fast cooling regime (fast cooling for the forward shock is important - X-ray luminosity for the termination shock and optical from the forward shock are comparable, (Margutti et al. 2019). But the expected spectrum will be non-thermal.

5. Non-thermal emission in FBOTs: pulsar-like termination shock in fast NS wind

5.1. Wind power

The newly created neutron star (NS) is spun up to short periods and magnetic field is amplified. The central NS will produce a highly magnetized wind that shocks against the ejecta (and, later on, against the pre-explosion wind). The NS wind-ejecta interaction will produce two shocks: forwards shock in the ejecta and termination shock in the wind. It is the wind termination shock that produces the X-ray emission, while the radiation-dominated forward shock produces the optical transient, see §4.2. In the termination shock the accelerated particles will produce synchrotron emission in the fast cooling regime, so that a large fraction of the wind power will be emitted as radiation. (See Lyutikov & Camilo Jaramillo 2017, for discussion of emission produced at the highly magnetized termination shock in GRBs).

In the fast cooling regime most of the power given to the accelerated particles is emitted. Let us then identify the observed X -ray luminosity with NS wind power. It is nearly constant at $L_0 \approx 10^{43}$ erg s⁻¹ until $t_{\Omega} \sim 20$ days and then falls $\propto t^{-2}$ (Fig. 5 in Margutti et al. 2019). Using the initial pulsar spin-down power and spin-down time t_{Ω} , we find the magnetic field and the initial spin

$$B_{NS} \approx \frac{c^{3/2} I_{NS}}{\sqrt{L_0} R_{NS}^3 t_{\Omega}} = 8 \times 10^{14} \,\mathrm{G}$$

$$\Omega_0 = \sqrt{\frac{L_0 t_{\Omega}}{I_{NS}}} = 140 \,\mathrm{rads}^{-1}$$
(18)

At $t > t_{\Omega}$ we have $L \propto t^{-2}$. Thus we suggest that a magnetar-type object is formed; its initial spin is not very high - 45 milliseconds. The wind power at time t is then

$$L_w = \frac{L_{w,0}}{(1 + t/t_{\Omega})^2} \tag{19}$$

(In fact, since observed X-ray luminosity is a lower limit on wind power, estimates (18) are upper limit on magnetic field and lower limit on the initial spin.

The dynamics of shock driven by the wind with power (19) will depend on two factors: spin-down time t_{Ω} and whether the shock is in the ejecta, §5.2, or in the pre-explosion wind, §5.3. We consider the two cases next.

5.2. Propagation of NS wind-driven shock through ejecta

The newly formed neutron star generates powerful wind that first propagates within the ejecta, and later on through the pre-explosion wind. Let us consider the dynamic of the wind-driven shock propagating through ejecta with density (4). In the Kompaneets approximation (Kompaneets 1960; Bisnovatyi-Kogan & Silich 1995) 1 , the relativistic wind with power L_{w} will produce a cavity expanding according to

$$\frac{L_w}{4\pi R^2 c} = \rho_{ej} \left(\partial_t R - \frac{R}{t} \right)^2 \tag{20}$$

Given the wind power (19) and density (4) the radius of the cavity evolves according to

$$R_{PWN} \approx \frac{(L_{w,0}t_{\Omega})^{1/4}V_{ej,0}^{3/4}}{(cM_{ej})^{1/4}}t\sqrt{\arctan\sqrt{t/t_{\Omega}}} = \begin{cases} \frac{L_{w,0}^{1/4}V_{ej,0}^{3/4}}{(cM_{ej})^{1/4}}t^{5/4}, & t \to 0\\ \sqrt{\frac{\pi}{2}}\frac{(L_{w,0}t_{\Omega})^{1/4}V_{ej,0}^{3/4}}{(cM_{ej})^{1/4}}t, & t \to \infty \end{cases}$$
(21)

(function $x\sqrt{\arctan\sqrt{x}}$ has limits $x^{5/4}$ for $x \ll 1$ and $\sqrt{\pi/2}x$ for $x \gg 1$). For example, at one day the neutron star produces a cavity if a size $R \approx 6 \times 10^{13} m_{ei,-2}^{-1/4}$.

The relative velocity of the shock with respect to the ejecta is

$$V_s = 0.37 \frac{(L_{w,0}t)^{1/4} V_{ej,0}^{3/4}}{(cM_{ej})^{1/4}} = 2 \times 10^8 t_d^{1/4} m_{ej,-2}^{1/4} \,\mathrm{cm}\,\mathrm{s}^{-1}$$
(22)

Thus, it changes only slowly with time.

The corresponding equipartition post-termination shock magnetic field (in the highly magnetized wind) is

$$B = \frac{\sqrt{2L_w}}{\sqrt{c}R} = \sqrt{2} \frac{L_{w,0}^{1/4} M_{ej}^{1/4}}{c^{1/4} V_{ej0}^{3/4}} \left(t^{5/4} \sqrt{1 + t/t_{\Omega}} \right)^{-1} \approx 300 \text{Gm}_{ej,-2}^{1/4} \left(t_d^{5/4} \sqrt{1 + 0.05t_d} \right)^{-1}$$
(23)

(t_d is time measured in days.) Thus, at early times magnetic field $B \propto t^{-5/4}$, while later $B \propto t^{-7/4}$.

Also note that the NS-driven shock never overtakes the freely expanding ejecta (radius (21) is always smaller than $V_{ej,0}t$). The shock breaks out hydrodynamically from the ejecta into the preexisting wind when ejecta starts to decelerate at (7), after approximately a month.

5.3. Propagation of NS wind-driven shock through pre-explosion wind

The Kompaneets approximation (20), in the pre-explosion wind profile (1) takes the form (see Appendix A for comparison with Sedov scaling - the resulting relations are similar)

$$\frac{L_w}{4\pi R^2 c} = \rho_w \left(\partial_t R - v_w\right)^2 \tag{24}$$

Using the wind power (19), Eq. (24) gives

$$R_{PWN} = tv_w + \sqrt{\frac{L_{w,0}v_w}{c\dot{M}}} t_\Omega \ln(1 + t/t_\Omega) \approx \sqrt{\frac{L_{w,0}v_w}{c\dot{M}}} t$$
 (25)

where the last relation assumes $t \ll t_{\Omega}$ and high shock velocity $V_s \gg v_w$.

$$V_s = \sqrt{\frac{L_{w,0}v_w}{c\dot{M}}} = 7 \times 10^8 V_{w,8}^{1/2} \dot{m}_{-3}^{-1/2} \text{cm s}^{-1}.$$
 (26)

¹Kompaneets approximation assumes supersonic driving, while Sedov scaling assumes subsonic driving of the expansion. At early times, when the termination shock is close to the contact discontinuity, the Kompaneets approximation is more justified that the Sedov's.

The equipartition magnetic field is

$$B \approx \frac{\sqrt{2L_w}}{\sqrt{cR}} = \sqrt{\frac{2\dot{M}}{v_w}} \frac{1}{t(1 + t/t_{\Omega})}$$
 (27)

Thus, at later times, for $t \gg t_{\Omega}$ magnetic field decreases $\propto t^{-2}$ (one power of time comes from radius increasing nearly linearly with time, another from decreasing central power).

5.4. The X-ray continuum and late NIR bump: synchrotron emission from the NS-driven termination shock

There are two separate components in the early X-ray spectrum: early, at $t_d \sim 7$, X-ray bump at ~ 50 keV and a continuous power-law. The bump disappeared later on, while the continuous component didn't show significant spectral evolution in the 0.3-10 keV during the 2 months Rivera Sandoval et al. (2018). In addition, after ~ 40 days there an increase in the NIR emission.

The continuous component is generally consisted with the synchrotron cooled population, resulting in the spectral index $\alpha \approx 0.5$. We associate the X-ray emission with the particles accelerated at the termination shock emitting in the fast cooling regime.

Suppose the neutron star-launched wind is propagating with Lorentz factor γ_w . The peak synchrotron frequency of particles accelerated by the wind termination shock is then, using the estimates of the magnetic field (23) and (27),

$$\epsilon_{s} \approx \gamma_{w}^{2} \hbar \frac{eB}{m_{e}c} = \begin{cases} \sqrt{2} \frac{e\hbar}{m_{e}c^{5/4}} \gamma_{w}^{2} \frac{L_{w,0} M_{ej}^{1/4}}{V_{ej,0}^{3/4}} \left(t^{5/4} \sqrt{1 + t/t_{\Omega}} \right)^{-1} = 50 \text{keV } m_{ej,-2}^{1/4} \gamma_{w,5}^{2} \left(t_{d}^{5/4} \sqrt{1 + 0.05t_{d}} \right)^{-1} \\ \frac{e\hbar}{m_{e}c} \gamma_{w}^{2} \sqrt{\frac{\dot{M}}{v_{w}}} \left(t(1 + t/t_{\Omega}) \right)^{-1} = 50 \text{keV } \dot{m}_{-3}^{1/2} v_{w,8} \gamma_{w,5}^{2} \left(t_{d} \sqrt{1 + 0.05t_{d}} \right)^{-1} \end{cases}$$
(28)

where t_d is time since explosion in days and first line corresponds to times when the shock is in the ejecta, while second when it is in the wind.

The cooling energy is

$$\epsilon_c \approx \frac{\hbar m_e^5 c^9}{e^7 R^2 t^2} \tag{29}$$

Initially it is very small, well below the injection frequency (28). As a result a cooled distribution will form below the injection peak, producing power-law spectrum with $\alpha \approx 0.5$. This is the origin of the persistent component. In the fast cooling regime the particle distribution below the injection peak is independent of the above-the-peak power-law distribution. This explains constant 0.3-10 keV spectrum (Rivera Sandoval et al. 2018) even for varying luminocity.

Later-on, with magnetic field in the termination shock decreasing $\propto t^{-2}$, Eq (27), the cooling energy increases sharply with time,

$$\epsilon_c \approx \frac{m_e^5 c^9 \hbar}{e^7} \frac{v_w^{3/2}}{\dot{M}^{3/2} t_{\Omega}^3} t^4$$
 (30)

(It is also a sensitive function of the parameters.). For faster, $v_w \sim 10^9 \text{ cm s}^{-1}$, and lighter, $\dot{M} \sim 10^{-4} M_{\odot}/\text{yr}$, early wind the cooling frequency reaches IR at times $t_d \sim 30$ days. As a result, injected particles will pile-up at the cooling energy. We suggest this as an origin of the late IR bump. ²

 $^{^2}$ Type-Ia SNe also show IR excess around ~ 30 days (e.g., Scalzo et al. 2019, Fig. 3). Given quite different environments, we assume that this similarity is superficial.

The early X-ray bump should have a somewhat separate origin: it cannot be produced by a constant injection source since in that case the spectrum will be of the broken power-law type ($\alpha = 0.5$ below the break and $\alpha = p/2$ above the break), not a spectral bump. We suggest that it is produced by an episode of injection - the estimate (28) for the injection energy early on matches the observed spectral peak.

6. Low frequency emission - free-free absorption in the ejecta and the wind

At lower frequencies, radio and IR waves can experience free-free absorption (Lang 1999, Eq. 1.223) both within the ejecta and in the pre-explosion wind.

Ejecta contribute to free-free absorption a lot

$$\tau_{ff,ej} = 2 \times 10^{20} m_{ej,-2}^4 \nu_{GHz}^{-4.2} T_4^{-2.7} t_d^{-10}$$
(31)

It is optically thin for very high frequencies for a long time

$$\nu_{GHz} > 7 \times 10^4 m_{ej,0.95} T_4^{-0.64} t_d^{-2.4} \tag{32}$$

Thus, in the radio and far IR the ejecta remains mostly opaque until the shock breakout from the ejecta, after approximately a month, Eq. (7).

The free-free optical depth through the wind, with density given by (1), becomes unity at

$$r_{ff,wind} = 1.5 \times 10^{16} \dot{m}_{-5}^{2/3} \nu_{GHz}^{-7/10} T_4^{-9/20} v_{w,8}^{-2/3}$$
(33)

The shock (21) reaches the optical depth of the order of unity through the pre-explosion wind, Eq (33), for

$$t = 8 \, \dot{m}_{-5}^{8/15} \nu_{GHz}^{-14/25} T_4^{-9/25} v_{w,8}^{-8/15} \, m_{ej,-2}^{1/5} {\rm days} \eqno(34)$$

The effects of free-free absorption explain the evolution of the radio and IR luminosities, see (Ho et al. 2019, Fig. 1). High frequencies, 341 and 230 GHz, are transparent all along, while lower frequency, 34 GHz traces the expanding radius of the corresponding $\tau = 1$ surface.

7. Population synthesis

7.1. Pre-merger evolutionary channels

Most calculations of WD-WD mergers are aimed at explaining the Type Ia SNe, thus *looking* for detonation (see Maoz et al. 2014, for a recent review). Less attention has been given to models that fail to detonate. As we argue, failed SN Ia, that collapse via electron capture, may be related to the FBOTs. Dan et al. (2014) discussed the results of the WD-WD mergers and argued that there is large phase space available for WD-WD mergers to produce an accretion induced collapse (AIC). Nomoto & Iben (1985) stressed the role of carbon ignition during WD mergers in order to produce a Type Ia SN. Thus, in order to avoid explosion, there should be little carbon in the system. We suggest then that the primary is a heavy ONeMg WD. In this section we calculate possible evolutionary scenarios and rates for the corresponding mergers.

We use the binary population synthesis (BPS) method to predict the properties of the binary mergers, that is the merger rates, host galaxies and formation channels. Using the BPS code SeBa (Portegies Zwart & Verbunt 1996;

Toonen et al. 2012; Toonen & Nelemans 2013), we simulate the evolution of a large number of binaries following in detail those that lead to the merger of an ONeMg and CO WD. Processes such as wind mass loss, stable & unstable mass transfer, accretion, angular momentum loss, and gravitational wave emission are taken into account. It was shown by Toonen et al. (2014) that the main source of uncertainty in the BPS outcomes come from the uncertainty in the input assumptions, in particular the CE-phase (CE stands for Common Envelope). For this reason, we follow Toonen et al. (2012), in performing two sets of population synthesis calculations using their model $\alpha\alpha$ and $\gamma\alpha$. For full details on the models, see Toonen et al. (2012). In short, these models differ from one another with respect to the modeling of the CE-phase. Despite the importance of this phase for the formation of compact binaries and the enormous effort of the community, the CE-phase is still poorly constrained (see Ivanova et al. 2013, for a review).

Commonly the CE-phase is modeled in BPS codes by energy conservation (Webbink 1984), with a parameter α that describes the efficiency with which orbital energy $E_{\rm orb}$ is consumed to unbind the CE, i.e.: $GM_dM_{d,env}/(\lambda R) = \alpha_{CE}(E_{orb,init} - E_{orb,final})$, where M_d is the mass of the donor star, $M_{d,env}$ the mass of its envelope, R its radius, λ the structure parameter of its envelope (Paczynski 1976; Webbink 1984; Livio & Soker 1988; de Kool et al. 1987; de Kool 1990). This recipe is used in model $\alpha\alpha$ for every CE-phase with alpha*lambda=2 (Nelemans et al. 2000).

This model is based on a balance of angular momentum with an efficiency parameter γ defined as $(J_{init} - J_{final})/J_{init} = \gamma M_{d,env}/(M_d + M_a)$, where J_{init} and J_{final} is the angular momentum of the pre- and post-mass transfer binary respectively, and M_a is the mass of the companion. This model is based on a balance of angular momentum with an efficiency parameter $\gamma = 1.5$ (Nelemans et al. 2000).

Figures 3-2 show the initial parameters of binaries leading to mergers between ONeMg and CO WDs in our simulations. Every point represents a single system in the BPS simulations. There are different evolutionary paths that can lead to an ONe-CO WD merger, however the two dominant channels consist of systems are: 1) the "inverted channel" (in blue circles) consists of systems with small initial semi-latus rectum $p \equiv a(1-e^2) < 200R_{\odot}$ for which the first phase of mass transfer is stable 2) systems in the "direct" channel (in green squares) are initially wider and evolve through a common-envelope phase. Typically the ONeMg-WD forms before the companion WD, whereas in the inverted channel the ONeMg WD is formed last (hence the name). For single stars, the initial mass of the progenitor of an ONeMg WD ranges between approximately $6.5-8M_{\odot}$ according to SeBa.This is similar to the range of initial masses in the direct channel where the initially most massive star (i.e. primary) forms the ONeMg WD (majority of green points in Fig. 3). The progenitors of ONeMg WDs in the "inverted" channel, i.e., the initially less massive star or secondary, denoted in blue, have lower masses initially as these stars accrete a significant amount of mass from their companion stars.

In Fig. 4 we show the final masses of the ONeMg and CO WD that merge according to model $\alpha\alpha$ and $\gamma\alpha$ respectively. The masses of the ONeMg WDs are in the range $1.1-1.4M_{\odot}$, while the majority of CO WDs have masses in the range $0.5\text{-}0.8\mathrm{M}_{\odot}$. As described above it is possible that the ONeMg WD forms before the other WD in the system (channel 'direct'), or it forms afterwards (channel 'inverted'). In model $\gamma\alpha$, 48% of merging ONe-CO DWDs go through the 'direct' channel, whereas for model $\alpha\alpha$ the fraction goes up to 69%. The masses of the CO WDs in the 'inverted' channel are systematically higher than those of the 'direct' channel.

In Fig. 5 we show the distribution of the mass ratio as a function of the primary mass at time of merger. For donor masses in the range $1.1 - 1.3 M_{\odot}$ Marsh et al. (2004) (see their Fig. 1) find that mass transfer is always unstable if the companion mass is above ~ 0.6 . It is always stable for $\leq 0.2 - 0.4$. The blue systems are well above the limit for unstable mass transfer. The green systems occupy a larger part of parameter space. The far majority of the systems have a mass ratio that make stable mass transfer unlikely. Also note that given the 'optimistic' stability limits of Marsh et al. (2004) the AM CVn rate is overestimated by orders of magnitude, indicating that mass transfer is likely less stable than the 'optimistic scenario'. In addition, the results from Marsh et al. (2004) do not take into account the effect of novae outbursts on the evolution of the systems. As shown by Shen et al. (2012) these outburst have a destabilizing

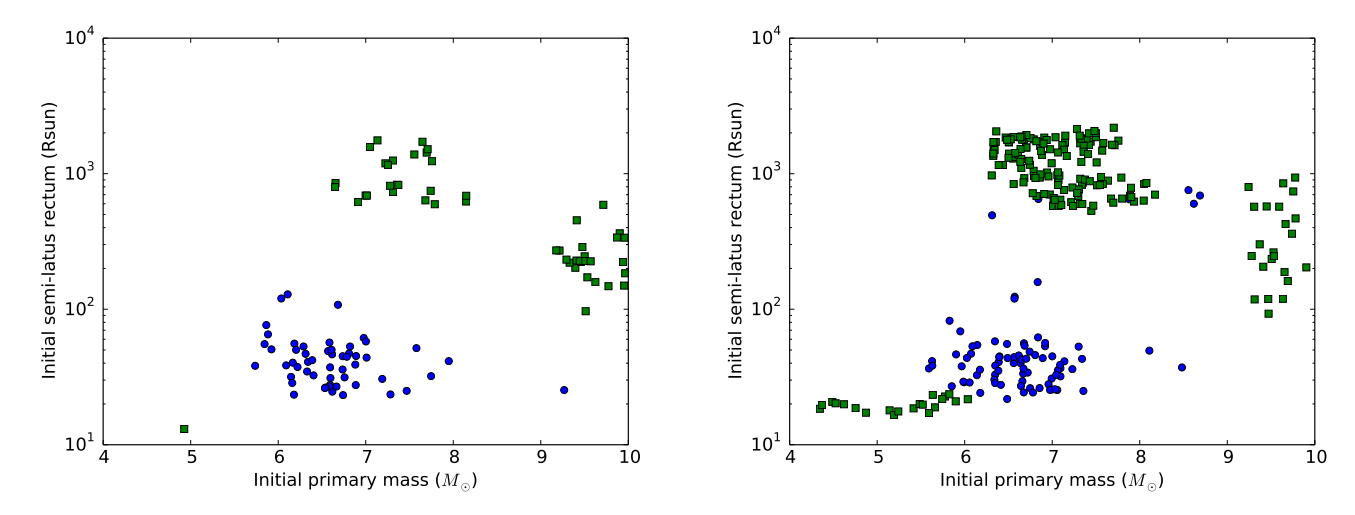


Fig. 2.— Distribution of initial semi-latus rectum for model $\gamma\alpha$ (left panel) and model $\alpha\alpha$ (right panel). The color coding is the same as in Fig. 3. In the case of $\alpha\alpha$, green dots at low orbital separations correspond to the systems in which the primary starts with $\sim 6M_{\odot}$ and relatively small separation, so that the first phase of mass transfer is stable. As the secondary accretes, it becomes more massive, its evolution speeds up, and it becomes a ONeMg WD while the primary is still a stripped (hydrogen poor helium-rich) nuclear burning star, which eventually becomes a WD. This is similar to the third evolution channel in Toonen et al. (2012).

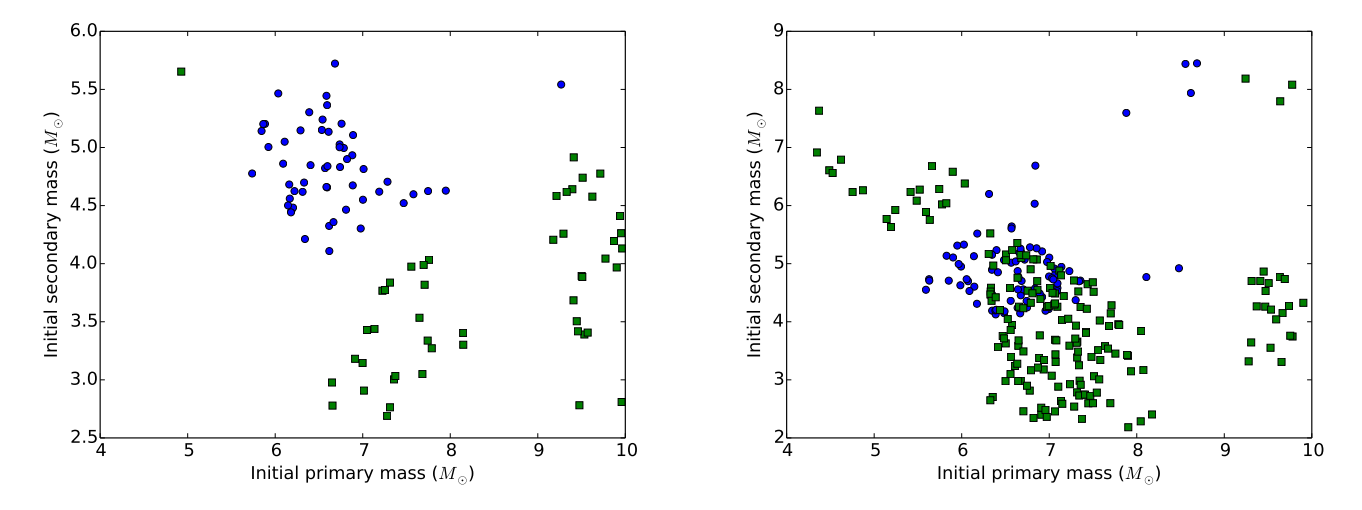


Fig. 3.— Distribution of initial masses for model $\gamma\alpha$ (left panel) and model $\alpha\alpha$ (right panel). The primary represents the first formed WD, secondary the last formed WD. With green squares the systems where the ONeMg WD is formed first, with blue circles where this is the last formed WD. In all models the systems marked in blue come from tight orbits where the first phase of mass transfer typically proceeds in a stable manner. The systems marked in green mostly originate from wider orbits, such that that first phase of mass transfer is likely a common-envelope phase.

effect on the mass transfer.

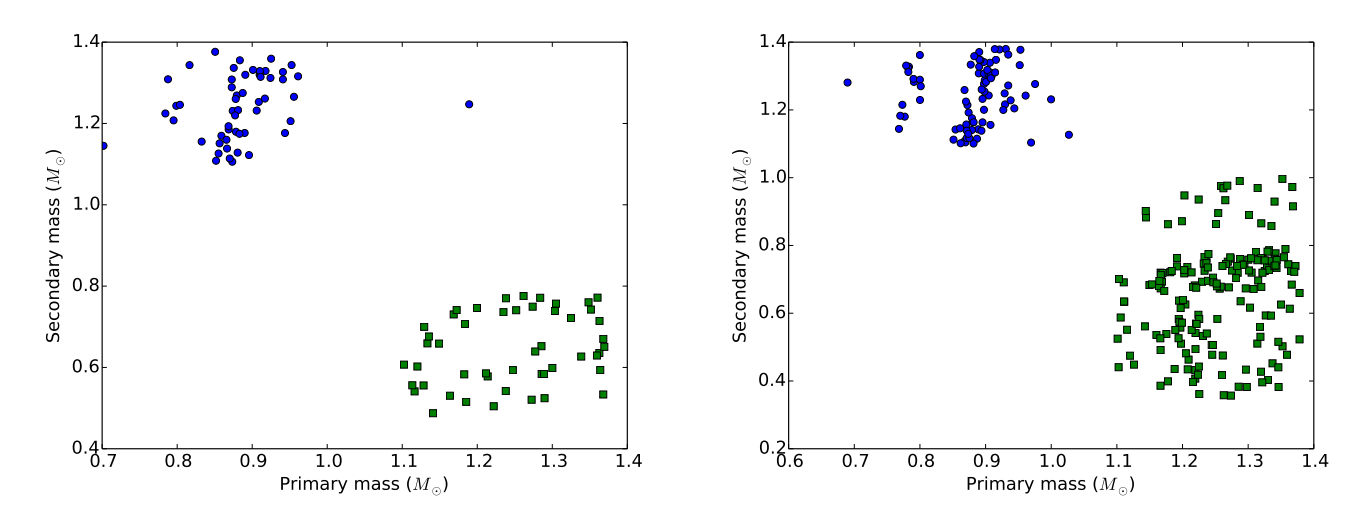


Fig. 4.— Distribution of WD masses for model $\gamma\alpha$ (left panel) and model $\alpha\alpha$ (right panel). The color coding is the same as in Fig. 3.

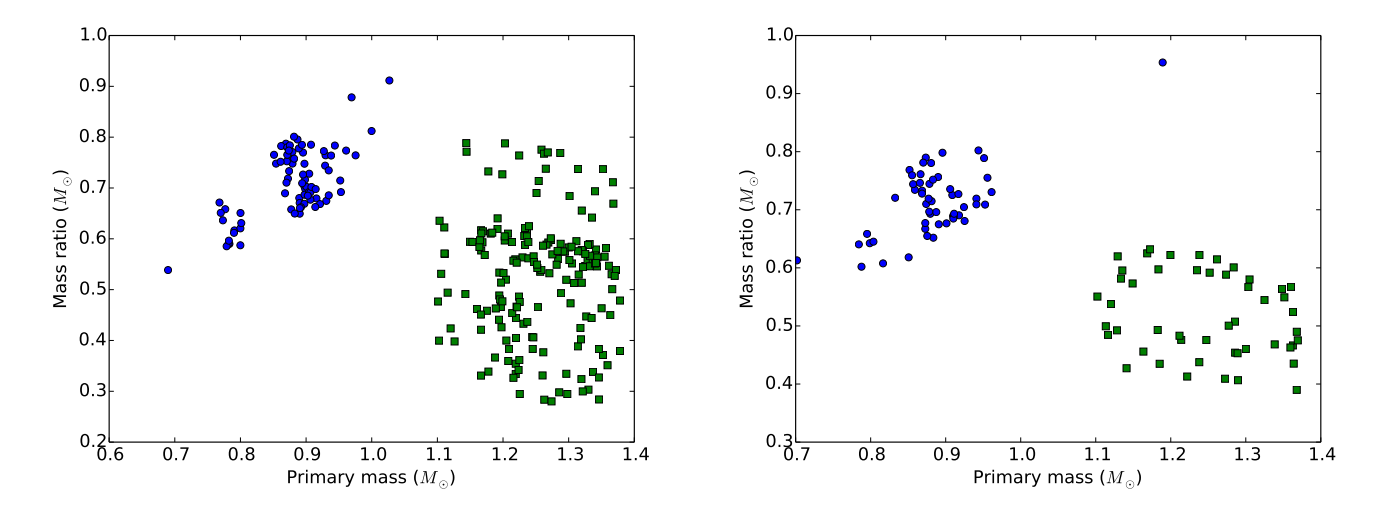


Fig. 5.— Distribution of the mass ratio as a function of the primary mass for model $\gamma \alpha$ (left panel) and model $\alpha \alpha$ (right panel). The color coding is the same as in Fig. 3.

7.2. Rates

Using the BPS simulations, we also estimate the rate of CO-ONeMg WD mergers. Assuming a constant star formation history of $4M_{\odot}$ yr⁻¹ for a Hubble time (roughly alike the Milky Way), the current merger rate ranges from $1.4 \times 10^{-4} \text{yr}^{-1}$ for model $\alpha \gamma$ and $3.4 \times 10^{-4} \text{yr}^{-1}$ for model $\alpha \alpha$. This is in agreement with the BPS calculations of Yungelson & Kuranov (2017) and Ruiter et al. (2019). The CO-ONeMg are less common than mergers between CO-CO WDs for which we find a merger rate of $4.5 \times 10^{-3} \text{yr}^{-1}$. Mergers of CO-CO WDs with a combined mass above Chandrasekhar, the double-degenerate progenitors model for supernova type Ia (Webbink 1984; Iben & Tutukov 1984), have a merger rate of $1.7 - 2.2 \times 10^{-3} \text{yr}^{-1}$ in our simulations, about an order of magnitude above that of CO-ONeMg

WDs.

Integrated over time, the total number of CO-ONeMg WD mergers ranging between $(3.5-8.6)\cdot 10^{-5}$ per Solar mass of created stars³. The rate of FBOTs has been estimated by Drout et al. (2014) to be 4%-7% of core-collapse supernova. Assuming the core-collapse rate is about $0.0025-0.010 {\rm M}_{\odot}^{-1}$ (Maoz & Graur 2017; Horiuchi et al. 2011; Graur et al. 2017)⁴, the estimated CO-ONeMg WD merger rate is consistent with the lower limit of the FBOT rate.

7.3. Host galaxies

In Fig. 6 we show the distributions of delay times of the CO-ONeMg mergers after a single burst of starformation. Their merger rates peaks at short delay times of about $\sim 50\text{-}100\text{Myr}$, with a long tail to long delay times. The peak occurs significantly earlier than expected from the classical type Ia supernovae progenitors consisting of superChandrasekhar mergers of CO-CO WDs (consistent with Yungelson & Kuranov 2017; Ruiter et al. 2019). The typical delay time of the CO-ONeMg mergers is closer to that of core-collapse supernovae, which peaks sharply at $\sim 50\text{Myr}$ (see e.g. Fig.3 of Zapartas et al. 2017). As a result, we expect the host galaxies of CO-ONeMg mergers to be more similar to those of core-collapse supernovae instead of Type Ia supernovae. This is consistent with the observed host galaxies of FBOTs (Drout et al. 2014).

8. Alternatives

An alternative to the WD merger scenario is the possibility of ultra-stripped envelopes in close binaries (Tauris et al. 2013, 2015). Binary interactions may strip the primary star of the envelope and also affect the mass of the collapsing core (Langer 2012; Podsiadlowski et al. 2004). Müller et al. (2018a,b) estimate that ultra-stripped SNe produce normal slowly rotating pulsars, which are unlikely to produce fast spinning central neutron star. Müller et al. (2018a) studied the case when the angular momentum is implanted onto the neutron star only due to accretion of a tenuous envelope, without accounting for the progenitor's initial spins. In contrast, in the case of double WD merger the envelope has a lot of angular momentum and has time to implant it to the core during the shell burning stage.

In a possibly related line of research, Piran & Shaviv (2005), see also Dall'Osso et al. (2014), argued that the pulsar J0737-3039B was born through non-standard SN mechanism (presumably via AIC), similar to the ultra-stripped case considered by Tauris et al. (2015). Piran & Shaviv (2005) also argued for slow initial spin (and slow kick velocity). Thus, ultra-stripped binary cores produce slowly rotating remnants, while AT2018cow needs a powerful central source.

9. Discussion

In this paper we discuss a channel for transient emission after electron-capture collapse to a neutron star following a merger of two WDs. Qualitatively, this channels allows a collapse into a neutron star to occur with a small envelope mass. As a result the ejecta is light, have high velocity and becomes optically transparent much earlier. This early transparency allows higher radiation efficiency, as energy is not spent on adiabatic expansion of the envelope. In AT2018cow the ejecta was the lightest, with only $\sim 10^{-2} M_{\odot}$ ejected. In this case the AIC occurred at the time when most of the envelope was

³This is independent of the assumed star formation history.

⁴The upper limit is calculated by Maoz & Graur (2017). The lower limit is based on the observed supernova type Ia rate ((1.3±0.1) $\dot{1}0^{-3}M_{\odot}^{-1}$ Maoz & Graur 2017) and the ratio of core-collapse to type Ia supernova (0.25-4 Graur et al. 2017)

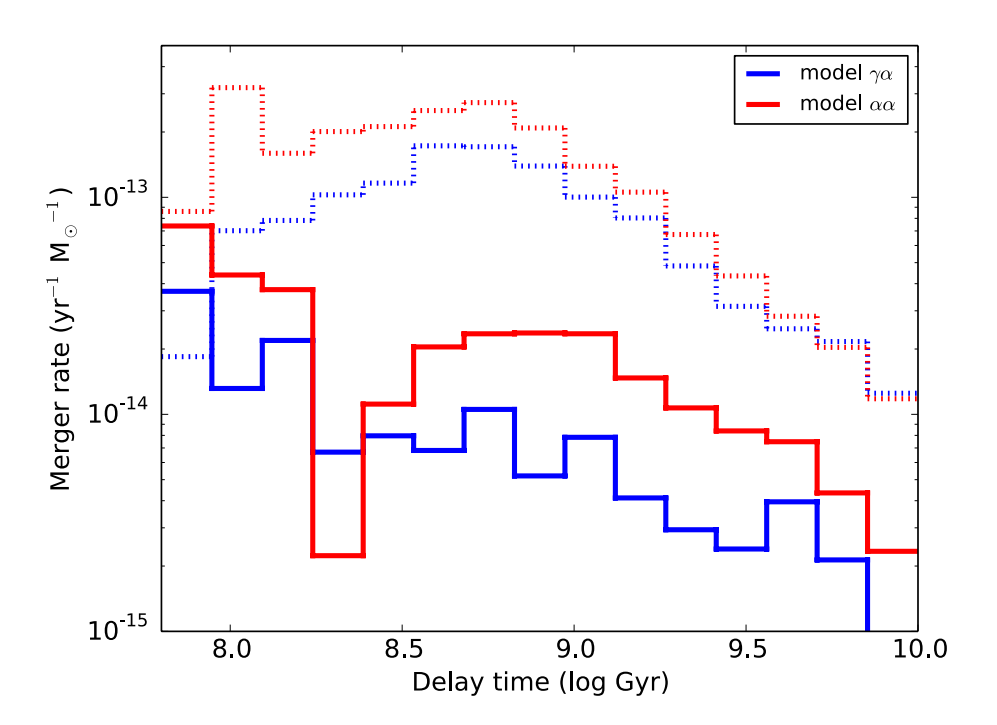


Fig. 6.— Delay time distribution of the CO-ONeMg WD mergers (solid lines) for two models of common-envelope evolution. Model $\gamma \alpha$ is shown is blue, and model $\alpha \alpha$ in red. For comparison the super-Chandrasekhar mergers of CO-CO WDs is shown with dotted lines. These typically occur at later delay times than the CO-ONeMg WD mergers.

already lost to the wind. Other FBOTs may have larger remaining envelopes at the moment of AIC and larger ejected masses, but all smaller than $\sim 0.5 M_{\odot}$. In our model the envelop mass depends on the mass of the primary ONeMg WD

(how close it is to the Chandrasekhar limit), and the mass of the companion (how quickly mass is added to the core, mass loss rate - how long the shell burning continues).

Let us highlight how the key observational results discussed by Margutti et al. (2019) are explained in our model

- A very short rise time to peak, $t_{\text{rise}} \sim \text{few days}$ optical transient is generated by an envelope ejected during the bounce from the proto-neutron star. Ejected mass is small, while velocity is nearly relativistic (of the order of the escape velocity from the surface of a proto-neutron star).
- Large bolometric peak luminosity as the ejecta becomes optically thin early on, a large fraction of the internal energy is emitted (as opposed to been spent on adiabatic expansion in conventional SN explosion).
- Persistent blue colors, with lack of evidence for cooling at $\delta t \gtrsim 30$ days later-on the emission starts to become dominated by the non-thermal particles accelerators at the termination shock.
- Large blackbody radius $R_{\rm bb} \sim 8 \times 10^{14}$ cm wind-driven cavity expands to these scales on time scales of few days, Eq. (21).
- Persistent optically thick UV/optical emission with no evidence for transition into a nebular phase emission is dominated by the radiation-modified forward shock.
- Abrupt change of the velocity of the material which dominates the emission at times ≥ 20 days the jet breaks through the ejecta and enters the pre-explosion wind, after time given by (7).
- NIR excess of emission the cooling energy at the termination shock moved to IR both due to decreasing magnetic field in the post-shock flow, Eq. (28) and discussion afterwards.
- The spectra evolve from a hot, blue, and featureless continuum around the optical peak, to very broad features
 this is a transition from radiation-modified forward shock at early time to regular matter-dominated forward
 shock, combined with emission from the termination shock.

In addition

- "Late-time optical spectra at t > 20 days show line widths of 4000 km s⁻¹ (0.01c, indicating substantially lower outflow velocities than at earlier times (when v = 0.1c), and an abrupt transition from very high velocity to lower velocity emitting material" (Margutti et al. 2019). We associate this transition with the moment when the NS-driven shock plows through the ejecta and enters the pre-collapse wind, Eq. (7). This is due to slowing down of the ejecta.
- There are indication of hydrogen in the spectrum after few weeks (Margutti et al. 2019): if the disrupted WD was of the DA type one does expect of the order of $10^{-4}M_{\odot}$ of hydrogen in the pre-collapse wind. This explains the late appearance of hydrogen lines, presumably when the NS-driven forward shock exits the ejecta and enters the pre-existing wind. We have no way of telling what the atmosphere of a post interaction WD will be. However, it is probable that the majority will be a DA, and therefore the rates would not be wildly different from the ones presented here. Also, in a DA WD hydrogen is limited to a narrow outer layer that will be stripped first during the merger and then mixed up in the envelope.
- Similar X-ray and optical luminosities are naturally explained as emission from forward and NS wind termination shocks (the latter in the fast cooling regime).

- The early X-ray spectral bump is also due to the passage of the peak frequency (late similar effect will produce an IR increase)
- Erratic inter-day variability of the X-ray emission (Ho et al. 2019) is hard to reproduce within the forward shock scenario (Lyutikov 2006b), since the forward shock emission properties depend on the *integrated* quantities (central engine total energy and total matter swept). But this variability can be reproduced within the internal shock paradigm: in the fast cooling regime, either by the changes of the wind properties of the central source (Lyutikov & Camilo Jaramillo 2017), minijets in the outflow (Lyutikov 2006a), or by Crab flare-like reconnection processes in the shocked pulsar wind (Clausen-Brown & Lyutikov 2012; Lyutikov et al. 2018).
- We associate both the high energy as well as radio emission not with the forward shock, as is the case in regular SNe (Weiler et al. 1986; Chevalier 1998), but with the reverse shock in the newly formed PWN. As a result, temporal evolution will be different.

Also note, that AIC with a formation of a neutron star is probably responsible for formation of young pulsars in globular clusters (Lyne et al. 1996). This is consistent with the present model.

The present model, connecting FBOTs to the merger of WDs, is related to the possibility that *some* short GRBs come from a similar channel of WD mergers (Lyutikov & Toonen 2017). The detection of gravitational waves associated with a GRB (Abbott et al. 2017) identifies mergers of neutron stars as the central engine. It is not clear at the moment whether this identification is generic to the whole class of short GRBs. As discussed by Lyutikov (2009); Lyutikov & Toonen (2017), there is a number of observational contradictions to the binary neutron star merger paradigm (like extended emission and late flares - both not seen in GW/GRB170817). One possibility that is still viable, is that some short GRBs originate from WD mergers. Several parameters may separate outcomes of WD mergers (e.g., FBOTs and short GRBs): masses of the merging WDs, the amount of the material lost to the wind, and the spin right before the AIC (so that AIC can either occur directly to a neutron star or with a formation of an accretion disk). For preferential intrinsic parameters and viewing angles (e.g., observer along the spin axis of the collapsing WD), we may see a short GRB, and, later on, an FBOT.

Acknowledgments

This work had been supported by DoE grant DE-SC0016369 and NASA grant 80NSSC17K0757.

We would like to thank Maxim Barkov, Deanne Coppejans, Robert Fisher, Ori Fox, Raffaella Margutti, Danny Milisavljevic, Amir Levinson, Eran Ofek, Amir Sharon, Liliana Rivera, Nir Shaviv and Thomas Tauris for discussions. We also thank Yegor Lyutikov for comments.

REFERENCES

Abbott, B. P., Abbott, R., Abbott, T. D., Acernese, F., Ackley, K., Adams, C., Adams, T., Addesso, P., Adhikari, R. X., Adya, V. B., & et al. 2017, Physical Review Letters, 119, 161101

Abdikamalov, E. B., Ott, C. D., Rezzolla, L., Dessart, L., Dimmelmeier, H., Marek, A., & Janka, H.-T. 2010, Phys. Rev. D, 81, 044012

Arnett, W. D. 1982, ApJ, 253, 785

Balsara, D. S., Fisker, J. L., Godon, P., & Sion, E. M. 2009, ApJ, 702, 1536

Belyaev, M. A., Rafikov, R. R., & Stone, J. M. 2013, ApJ, 770, 67

Bisnovatyi-Kogan, G. S., & Silich, S. A. 1995, Reviews of Modern Physics, 67, 661

Brooks, J., Schwab, J., Bildsten, L., Quataert, E., Paxton, B., Blinnikov, S., & Sorokina, E. 2017, ApJ, 850, 127

Budnik, R., Katz, B., Sagiv, A., & Waxman, E. 2010, ApJ, 725, 63

Canal, R., & Schatzman, E. 1976, A&A, 46, 229

Chevalier, R. A. 1998, ApJ, 499, 810

Clausen-Brown, E., & Lyutikov, M. 2012, MNRAS, 426, 1374

Dall'Osso, S., Piran, T., & Shaviv, N. 2014, MNRAS, 438, 1005

Dan, M., Rosswog, S., Brüggen, M., & Podsiadlowski, P. 2014, MNRAS, 438, 14

de Kool, M. 1990, ApJ, 358, 189

de Kool, M., van den Heuvel, E. P. J., & Pylyser, E. 1987, A&A, 183, 47

Drout, M. R., Chornock, R., Soderberg, A. M., Sanders, N. E., McKinnon, R., Rest, A., Foley, R. J., Milisavljevic, D., Margutti, R., Berger, E., Calkins, M., Fong, W., Gezari, S., Huber, M. E., Kankare, E., Kirshner, R. P., Leibler, C., Lunnan, R., Mattila, S., Marion, G. H., Narayan, G., Riess, A. G., Roth, K. C., Scolnic, D., Smartt, S. J., Tonry, J. L., Burgett, W. S., Chambers, K. C., Hodapp, K. W., Jedicke, R., Kaiser, N., Magnier, E. A., Metcalfe, N., Morgan, J. S., Price, P. A., & Waters, C. 2014, ApJ, 794, 23

Fryer, C., Benz, W., Herant, M., & Colgate, S. A. 1999, ApJ, 516, 892

Graur, O., Bianco, F. B., Huang, S., Modjaz, M., Shivvers, I., Filippenko, A. V., Li, W., & Eldridge, J. J. 2017, ApJ, 837, 120

Ho, A. Y. Q., Phinney, E. S., Ravi, V., Kulkarni, S. R., Petitpas, G., Emonts, B., Bhalerao, V., Blundell, R., Cenko, S. B., Dobie, D., Howie, R., Kamraj, N., Kasliwal, M. M., Murphy, T., Perley, D. A., Sridharan, T. K., & Yoon, I. 2019, ApJ, 871, 73

Höflich, P., Wheeler, J. C., & Thielemann, F. K. 1998, ApJ, 495, 617

Horiuchi, S., Beacom, J. F., Kochanek, C. S., Prieto, J. L., Stanek, K. Z., & Thompson, T. A. 2011, ApJ, 738, 154

Iben, Jr., I., & Tutukov, A. V. 1984, ApJS, 54, 335

Inogamov, N. A., & Sunyaev, R. A. 1999, Astronomy Letters, 25, 269

—. 2010, Astronomy Letters, 36, 848

Ioka, K., Levinson, A., & Nakar, E. 2018, arXiv e-prints

Ito, H., Levinson, A., Stern, B. E., & Nagataki, S. 2018, MNRAS, 474, 2828

Ivanova, N., Justham, S., Chen, X., De Marco, O., Fryer, C. L., Gaburov, E., Ge, H., Glebbeek, E., Han, Z., Li, X.-D., Lu, G., Marsh, T., Podsiadlowski, P., Potter, A., Soker, N., Taam, R., Tauris, T. M., van den Heuvel, E. P. J., & Webbink, R. F. 2013, A&A Rev., 21, 59

Jones, S., Röpke, F. K., Pakmor, R., Seitenzahl, I. R., Ohlmann, S. T., & Edelmann, P. V. F. 2016, A&A, 593, A72

Karp, A. H., Lasher, G., Chan, K. L., & Salpeter, E. E. 1977, ApJ, 214, 161

Kashyap, R., Haque, T., Lorén-Aguilar, P., García-Berro, E., & Fisher, R. T. 2018, arXiv e-prints

Kitaura, F. S., Janka, H.-T., & Hillebrandt, W. 2006, A&A, 450, 345

Kompaneets, A. S. 1960, Soviet Physics Doklady, 5, 46

Landau, L. D., & Lifshitz, E. M. 1959, Fluid mechanics

Lang, K. R. 1999, Astrophysical formulae

Langer, N. 2012, ARA&A, 50, 107

Livio, M., & Soker, N. 1988, ApJ, 329, 764

Lyne, A. G., Manchester, R. N., & D'Amico, N. 1996, ApJ, 460, L41

Lyutikov, M. 2006a, MNRAS, 369, L5

- —. 2006b, New Journal of Physics, 8, 119
- —. 2009, ArXiv e-prints
- —. 2018, MNRAS, 477, 816

Lyutikov, M., & Camilo Jaramillo, J. 2017, ApJ, 835, 206

Lyutikov, M., Komissarov, S., & Sironi, L. 2018, Journal of Plasma Physics, 84, 635840201

Lyutikov, M., & Toonen, S. 2017, ArXiv e-prints

Maoz, D., & Graur, O. 2017, ApJ, 848, 25

Maoz, D., Mannucci, F., & Nelemans, G. 2014, ARA&A, 52, 107

Margutti, R., Metzger, B. D., Chornock, R., Vurm, I., Roth, N., Grefenstette, B. W., Savchenko, V., Cartier, R., Steiner, J. F., Terreran, G., Margalit, B., Migliori, G., Milisavljevic, D., Alexander, K. D., Bietenholz, M., Blanchard, P. K., Bozzo, E., Brethauer, D., Chilingarian, I. V., Coppejans, D. L., Ducci, L., Ferrigno, C., Fong, W., Götz, D., Guidorzi, C., Hajela, A., Hurley, K., Kuulkers, E., Laurent, P., Mereghetti, S., Nicholl, M., Patnaude, D., Ubertini, P., Banovetz, J., Bartel, N., Berger, E., Coughlin, E. R., Eftekhari, T., Frederiks, D. D., Kozlova, A. V., Laskar, T., Svinkin, D. S., Drout, M. R., MacFadyen, A., & Paterson, K. 2019, ApJ, 872, 18

Marsh, T. R., Nelemans, G., & Steeghs, D. 2004, MNRAS, 350, 113

Michel, F. C. 1973, ApJ, 180, L133

Miyaji, S., Nomoto, K., Yokoi, K., & Sugimoto, D. 1980, PASJ, 32, 303

Mösta, P., Ott, C. D., Radice, D., Roberts, L. F., Schnetter, E., & Haas, R. 2015, Nature, 528, 376

Müller, B., Gay, D. W., Heger, A., Tauris, T. M., & Sim, S. A. 2018a, MNRAS, 479, 3675

Müller, B., Tauris, T. M., Heger, A., Banerjee, P., Qian, Y.-Z., Powell, J., Chan, C., Gay, D. W., & Langer, N. 2018b, ArXiv e-prints

Nelemans, G., Verbunt, F., Yungelson, L. R., & Portegies Zwart, S. F. 2000, A&A, 360, 1011

Nomoto, K., & Iben, Jr., I. 1985, ApJ, 297, 531

Nomoto, K., & Kondo, Y. 1991, ApJ, 367, L19

Ofek, E. O., Rabinak, I., Neill, J. D., Arcavi, I., Cenko, S. B., Waxman, E., Kulkarni, S. R., Gal-Yam, A., Nugent, P. E., Bildsten, L., Bloom, J. S., Filippenko, A. V., Forster, K., Howell, D. A., Jacobsen, J., Kasliwal, M. M., Law, N., Martin, C., Poznanski, D., Quimby, R. M., Shen, K. J., Sullivan, M., Dekany, R., Rahmer, G., Hale, D., Smith, R., Zolkower, J., Velur, V., Walters, R., Henning, J., Bui, K., & McKenna, D. 2010, ApJ, 724, 1396

Paczynski, B. 1976, in IAU Symposium, Vol. 73, Structure and Evolution of Close Binary Systems, ed. P. Eggleton, S. Mitton, & J. Whelan, 75

Perley, D. A., Mazzali, P. A., Yan, L., Cenko, S. B., Gezari, S., Taggart, K., Blagorodnova, N., Fremling, C., Mockler, B., Singh, A., Tominaga, N., Tanaka, M., Watson, A. M., Ahumada, T., Anupama, G. C., Ashall, C., Becerra, R. L., Bersier, D., Bhalerao, V., Bloom, J. S., Butler, N. R., Copperwheat, C., Coughlin, M. W., De, K., Drake, A. J., Duev, D. A., Frederick, S., Jesús González, J., Goobar, A., Heida, M., Ho, A. Y. Q., Horst, J., Hung, T., Itoh, R., Jencson, J. E., Kasliwal, M. M., Kawai, N., Kulkarni, S. R., Kumar, B., Kumar, H., Kutyrev, A. S., Khanam, T., Lee, W. H., Maeda, K., Mahabal, A., Murata, K. L., Neill, J. D., Ngeow, C.-C., Penprase, B., Pian, E., Quimby, R., Ramirez-Ruiz, E., Richer, M., Román-Zúñiga, C. G., Srivastava, S., Socia, Q., Sollerman, J., Tachibana, Y., Taddia, F., Tinyanont, K., Troja, E., Ward, C., & Wee, J. 2018, ArXiv e-prints

Philippov, A. A., Rafikov, R. R., & Stone, J. M. 2016, ApJ, 817, 62

Pinto, P. A., & Eastman, R. G. 2000, ApJ, 530, 757

Piran, T. 2004, Reviews of Modern Physics, 76, 1143

Piran, T., & Shaviv, N. J. 2005, Physical Review Letters, 94, 051102

Podsiadlowski, P., Langer, N., Poelarends, A. J. T., Rappaport, S., Heger, A., & Pfahl, E. 2004, ApJ, 612, 1044

Portegies Zwart, S. F., & Verbunt, F. 1996, A&A, 309, 179

Prentice, S. J., Maguire, K., Smartt, S. J., Magee, M. R., Schady, P., Sim, S., Chen, T.-W., Clark, P., Colin, C., Fulton, M., McBrien, O., ONeill, D., Smith, K. W., Ashall, C., Chambers, K. C., Denneau, L., Flewelling, H. A., Heinze, A., Holoien, T. W.-S., Huber, M. E., Kochanek, C. S., Mazzali, P. A., Prieto, J. L., Rest, A., Shappee, B. J., Stalder, B., Stanek, K. Z., Stritzinger, M. D., Thompson, T. A., & Tonry, J. L. 2018, ApJ, 865, L3

Rivera Sandoval, L. E., Maccarone, T. J., Corsi, A., Brown, P. J., Pooley, D., & Wheeler, J. C. 2018, MNRAS, 480, L146

Ruiter, A. J., Ferrario, L., Belczynski, K., Seitenzahl, I. R., Crocker, R. M., & Karakas, A. I. 2019, MNRAS, 484, 698

Scalzo, R. A., Parent, E., Burns, C., Childress, M., Tucker, B. E., Brown, P. J., Contreras, C., Hsiao, E., Krisciunas, K., Morrell, N., Phillips, M. M., Piro, A. L., Stritzinger, M., & Suntzeff, N. 2019, MNRAS, 483, 628

Schwab, J., Quataert, E., & Bildsten, L. 2016, MNRAS, 458, 3613

Sharon, A., & Kushnir, D. 2019, arXiv e-prints

Shen, K. J., Bildsten, L., Kasen, D., & Quataert, E. 2012, ApJ, 748, 35

Smartt, S. J., Clark, P., Smith, K. W., McBrien, O., Maguire, K., O'Neil, D., Fulton, M., Magee, M., Prentice, S., Colin, C., Tonry, J., Denneau, L., Stalder, B., Heinze, A., Weiland, H., Flewelling, H., & Rest, A. 2018, The Astronomer's Telegram, 11727

Svirski, G., & Nakar, E. 2014, ApJ, 788, 113

Tauris, T. M., Langer, N., Moriya, T. J., Podsiadlowski, P., Yoon, S.-C., & Blinnikov, S. I. 2013, ApJ, 778, L23

Tauris, T. M., Langer, N., & Podsiadlowski, P. 2015, MNRAS, 451, 2123

Timmes, F. X., & Woosley, S. E. 1992, ApJ, 396, 649

Toonen, S., Claeys, J. S. W., Mennekens, N., & Ruiter, A. J. 2014, A&A, 562, A14

Toonen, S., & Nelemans, G. 2013, A&A, 557, A87

Toonen, S., Nelemans, G., & Portegies Zwart, S. 2012, A&A, 546, A70

Toonen, S., Perets, H. B., Igoshev, A. P., Michaely, E., & Zenati, Y. 2018, A&A, 619, A53

Weaver, T. A. 1976, ApJS, 32, 233

Webbink, R. F. 1984, ApJ, 277, 355

Weiler, K. W., Sramek, R. A., Panagia, N., van der Hulst, J. M., & Salvati, M. 1986, ApJ, 301, 790

Woosley, S. E., & Baron, E. 1992, ApJ, 391, 228

Yungelson, L. R., & Kuranov, A. G. 2017, MNRAS, 464, 1607

Zapartas, E., de Mink, S. E., Izzard, R. G., Yoon, S.-C., Badenes, C., Götberg, Y., de Koter, A., Neijssel, C. J., Renzo, M., Schootemeijer, A., & Shrotriya, T. S. 2017, A&A, 601, A29

A. Sedov approximation for dynamics of pulsar-driven wind propagating through pre-explosion wind

Another analytical scaling for the dynamics of the strong shock is due to Sedov, which assumes energy conservation (as opposed to momentum flux conservation in case of Kompaneets approximation). Consider first times shorter than spin-down time $t \ll t_{\Omega}$. In the thin shell limit, the energy in the swept-up shell is the energy deposited into the shell by the central source, L_0t plus the kinetic energy of the swept-up matter $M_{swept}v_w^2/2$ where $M_{swept} = 4\pi r r_0^2 \rho_0$ is the swept-up mass (assuming cold wind with constant velocity),

$$L_0 t + 4\pi r r_0^2 v_w^2 \rho_0 = 4\pi r r_0^2 \rho_0 v^2 / 2 \tag{A1}$$

Dimensionalizing

$$L_0 = l_0 2\pi r_0^3 v_w^2 / 2$$

$$t = \tilde{t}(r_0 / v_w)$$

$$r = \tilde{r}r_0$$
(A2)

This preprint was prepared with the AAS LATEX macros v5.2.

we find

$$l_0\tilde{t} + \tilde{r} = \tilde{r}\dot{\tilde{r}}^2 \tag{A3}$$

At early time, neglecting the accumulated energy of the wind, $l_0 \tilde{t} \gg \tilde{r}$

$$\tilde{r} = l_0^{1/3} \tilde{t}$$

$$r = \frac{L_0^{1/3} t}{2\pi^{1/3} \rho_0^{1/3} r_0^{2/3}} = \frac{2^{1/3} L_0^{1/3} v_w^{1/3}}{\dot{M}^{1/3}} t$$

$$V_{s,S} \approx \frac{L_0^{1/3} v_w^{1/3}}{\dot{M}^{1/3}}$$
(A4)

Comparing with the Kompaneets approximation, Eq. A5,

$$\frac{V_s}{V_{s,S}} \approx c^{1/2} \left(\frac{\dot{M}}{L_0 v_w}\right)^{1/6} = 3.6 \dot{M}_{-3}^{1/6} v_{w,8}^{-1/6}$$
(A5)

Thus, both Sedov's and Kompaneets's approximations give similar estimates for the shock dynamics at this time.

At times much longer than the spin-down time, $t \gg t_{\Omega}$, the central engine has deposited most of it's energy in the shock, so that energy conservation gives

$$E_0 + 4\pi r r_0^2 v_w^2 \rho_0 = 4\pi r r_0^2 \rho_0 v^2 / 2 \tag{A6}$$

with $E_0 = L_0 t_{\Omega}$. Dimensionalizing

$$\epsilon_0 = \frac{E_0}{4\pi r_0^3 v_w^2 / 2} \tag{A7}$$

The energy conservation now takes the form

$$\epsilon_0 + \tilde{r} = \tilde{r}\dot{\tilde{r}}^2$$

$$\epsilon_0 = \frac{E_0}{4\pi r_0^3 v_w^2/2}$$
(A8)

with a solution

$$\tilde{t} = \sqrt{\tilde{r}(\epsilon_0 + \tilde{r})} + \epsilon_0 \ln \frac{\sqrt{\epsilon_0}}{\sqrt{\tilde{r}} + \sqrt{\epsilon_0 + \tilde{r}}}$$
(A9)

At times when the swept-up kinetic energy is not significant,

$$\tilde{r} = (3/2)^{2/3} \epsilon_0^{1/3} \tilde{t}^{2/3}$$

$$r = \frac{3^{2/3} E_0^{1/3} t^{2/3}}{2\pi^{1/3} \rho_0^{1/3} r_0^{2/3}} = \frac{3^{2/3}}{2^{1/3}} \frac{E_0^{1/3} v_w^{1/3}}{\dot{M}^{1/3}} t^{2/3}$$
(A10)

where the last two relation assume $r \to 0$ limit.